Vietnam Journal of Science and Technology
DOI: https://doi.org/10.15625/2525-2518/20279

Structural characterization and electrochemical properties of MoS_2/graphene oxide nanocomposite for supercapacitor application

Le Ngoc Long[1,2,3], Tran Van Khai[1,2,4,*]

[1]*Faculty of Materials Technology, Ho Chi Minh City University of Technology (HCMUT), 268 Ly Thuong Kiet street, Dien Hong ward, Ho Chi Minh City, Viet Nam*
[2]*Vietnam National University - Ho Chi Minh City (VNU-HCM), Quarter 33, Linh Xuan ward, Ho Chi Minh City, Viet Nam*
[3]*School of Applied Chemistry, Tra Vinh University, 126 Nguyen Thien Thanh street, Hoa Thuan ward, Vinh Long Province, Viet Nam*
[4]*VNU-HCM Key Laboratory for Material Technologies, Ho Chi Minh City University of Technology (HCMUT), 268 Ly Thuong Kiet street, Dien Hong ward, Ho Chi Minh City, Viet Nam*

*Email: *tvkhai1509@hcmut.edu.vn*

Received: 6 March 2024; Accepted for publication: 25 July 2024

Abstract. Supercapacitors and micro-supercapacitors are promising capacitive energy storage devices for portable electronics and microelectromechanical systems. However, their low volumetric energy and power density as compared to batteries might limit them from many practical applications. In this research, the low-dimension MoS_2/graphene oxide nanocomposite (MoS_2/C NC) was successfully synthesized by a simple hydrothermal approach and utilized it as an electrode material for supercapacitor applications. The obtained materials were systematically investigated by various characterization techniques. Field emission scanning electron microscopy (FE-SEM) and high-resolution transmission electron microscopy (HR-TEM) were used to evaluate surface morphology, microstructure and crystallite size; while the X-ray diffraction (XRD), energy-dispersive X-ray spectroscopy (EDS), X-ray photoelectron spectroscopy (XPS), Fourier transform infrared (FTIR) and Raman spectroscopy were used to analyze phase and chemical composition of the synthesized samples. The electrochemical capacitance properties were measured by cyclic voltammetry (CV) and electrochemical impedance spectroscope (EIS) techniques. From FE-SEM and HR-TEM results, it was evident that ultrathin two-dimensional (2D) MoS_2 crystals were in-situ grown on the graphene oxide surface, resulting in rich porous three-dimensional (3D) architecture. The thickness and average lateral size of MoS_2 crystals by HRTEM were around ~1.8–3.5 nm (~3–6 nm layers) and ~200–300 nm, respectively. The results of XRD, Raman, and XPS studies confirm that the as-grown MoS_2 crystals have a predominantly hexagonal phase structure (2H-MoS_2). Interestingly, thin film electrode prepared from the MoS_2/C NC shows a high specific capacitance of ~118.5 F g^{-1} under 1 A g^{-1} with electrochemical active surface area of ~218.0 m^2 g^{-1}. The obtained high energy density of ~88.0 Wh kg^{-1} and a power density of ~367.0 W kg^{-1}, along with low charge transfer resistance of the synthesized MoS_2/C NC which make it a promising candidate for supercapacitor applications.

Keywords: MoS_2, graphene, nanocomposite, electrochemical, supercapacitor.

Classification numbers: 2.4.4, 2.8.3, 2.9.4.

1. INTRODUCTION

Controlling the electrostatic charge and discharge of the electrochemical double layer at the electrode-electrolyte surfaces of high specific surface area materials is important for energy storage devices such as supercapacitors. Supercapacitors store energy by forming a charged double layer of electrolyte ions on the surface of the electrode materials [1]. Therefore, the charge density or energy density of a supercapacitor depends mainly on the surface area of the electrode materials. Factors that affect the performance of supercapacitors including electrode materials, separators, electrolytes, and fabrication techniques [2]. Among these mentioned parameters, electrode materials are a main factor that strongly influences the capacitance and energy density of the supercapacitors. Therefore, one of the effective methods to increase the energy density of supercapacitors is to use electrode materials with high specific surface area.

In this regard, graphene, a monolayer of carbon atoms covalent bond together by sp^2 hybridization in a hexagonal crystalline lattice, has gained much attention due to its attractive physicochemical properties [3], including high charged carrier mobility of ~2×10^5 cm^2 V^{-1} s^{-1} [4, 5], high specific surface area of ~2630 m^2 g^{-1} [6], and semi-metallic properties with zero bandgap [5] that necessary for controlling the electrostatic charge and discharge of the double layer formed at their contact interface with electrolytes medium. Such interesting physical properties that turn graphene to become a promising platform for various applications including fuel cells [7], Li-ion batteries [8, 9], and supercapacitors [10]. Unfortunately, graphene exhibits low efficiency in supercapacitors due to its insufficiency charge-storage capability.

Recently, molybdenum disulfide (MoS_2) has emerged as one of the most attractive two-dimensional (2D) materials belongs to the transition-metal dichalcogenide (TMDs) group [11]. Similar to graphene, 2D-MoS_2 possesses a lamellar structure in which Mo atoms are covalently bonded to S atoms forming a 2D monolayer of S–Mo–S. These monolayers stack on each other via weak van der Waals interactions along the [001] direction to form MoS_2 crystals [12]. MoS_2 exhibits its charge storage capability by forming electric double-layers of charged carriers at their contact interface with electrolytic medium (double-layer capacitance mechanism) and by faradaic charge transfer interlayer or intralayer on the Mo centers whose oxidation states can occupy between +2 and +6 (pseudo-capacitance mechanism). These characteristics result in significant high energy density for supercapacitor applications with unlimited charging/discharging cycles. Nevertheless, low carrier mobility of 2D-MoS_2 (~0.5–3.0 cm^2 V^{-1} s^{-1}) material limits most of its efficiency in such energy storage devices as batteries or supercapacitance [13]. Very recently, the incorporation of MoS_2 into graphene or graphene oxide (GO) have gained a great deal of interest due to their improved performance and stability in a variety of area, from energy storage/conversion to biomedical applications [14-17]. It is expected that the combination of two these materials from van der Waals solids or from the covalent bonding materials will allow full use of their advantages and mitigate their disadvantages [18]. Currently, various methods have been developed to synthesize MoS_2/graphene composites, such as solvothermal [19], hydrothermal [14, 15, 20], chemical vapor deposition (CVD) [21], van der Waals epitaxy [22], sonication [23], microwave [24], and liquid-phase exfoliation [31]. Among them, hydrothermal method is a most common method to prepare MoS_2/graphene nanocomposites. It has the advantages of relatively low temperatures and pressures, uniform mixing of raw materials, and allows precise control over the morphology and size of MoS_2 and graphene components. The method is also suitable for large-scale production and enables the formation of well-dispersed MoS_2 on graphene sheets, enhancing interfacial interactions and material properties. Therefore, it is expected to become one of the primary approaches for industrial production of high-

performance MoS_2/graphene nanocomposites. In this research, we proposed a simple hydrothermal synthesis approach in which nanostructured 2D-MoS_2 crystals were grown on GO nanosheets to produce MoS_2/C NC material. We then studied the specific capacitance and electrochemical characteristics of a thin film electrode made from the resulting MoS_2/C NC for supercapacitor applications. Interestingly, integrating 2D-MoS_2 nanocrystalline structures into the GO matrix resulted in a considerable improvement in the specific capacitance of the produced MoS_2/C NC electrode, along with great cycle stability and low electrical resistance. This opens up the prospect of its employment in supercapacitor applications.

2. MATERIALS AND METHODS

2.1. Chemicals

Graphite flakes (99.8 %) was commercially obtained from Sigma Aldrich (St. Louis, MO, USA). Sulfuric acid (H_2SO_4, 98 %), phosphoric acid (H_3PO_4, 85 %), potassium permanganate ($KMnO_4$, 98 %), hydrogen peroxide (H_2O_2, 30 wt. %), molybdate tetrahydrate ($(NH_4)_6Mo_7O_{24}.4H_2O$, 98 %), thioacetamide (CH_3CSNH_2, 98 %), ammonia solution (NH_4OH, 25 wt%) were purchased from Merck Chemicals Co. Ltd, Germany. All the reagents used in the experiments were analytical grade and used without further purification.

2.2. Synthesis of MoS_2/graphene oxide nanocomposites (MoS_2/C NCs)

In this work, in the first step, the GO nanosheets were synthesized from the chemial oxidation of graphite flakes with $KMnO_4$ in a mixture solution containing H_2SO_4 and H_3PO_4. Details of the GO synthesis process are presented in [25-28]. Then, the MoS_2/graphene oxide nanocomposites (MoS_2/C NCs) with molar ratio of Mo^{4+} (~1.5):C (~1) were synthesized by a simple hydrothermal technique. Briefly, an amount of ~0.1506 gram of $(NH_4)_6Mo_7O_{24}.4H_2O$ and 0.3069 gram of CH_3CSNH_2 were added to a volume ~100 mL of GO (~1.0 g L^{-1}) dispersion, and then submitted to ultrasonication in bath water for ~1 h (at 37 kHz, kept at ~30 °C), resulting in a homogeneous suspension. The obtained suspension then was adjusted to pH of ~5–6 by addition of an appropriate volume of NH_3 solution. Next, the mixture was put into a 125 mL Teflon-lined stainless steel autoclave reactor (Parr Instrument Company, Moline, IL, USA, ~80 % volume filled) and heated at 230 °C for 2 h with a heating rate of ~10 °C/min. After that, the autoclave reactor was removed from the furnace and allowed to cool naturally to ambient temperature. Then, the synthesized products were washed multiple times with deionised water and ethanol solution before being collected by centrifugation. Finally, the resultant products were dried in a vacuum furnace at 60 °C for 24 hours before being utilized to characterize the properties. For comparison purpose, the bare MoS_2 nanocrystals was also synthesized under the same conditions, with the exception of adding the GO dispersion in the precursor.

2.3. Characterization

2.3.1. Structure and morphology

The crystal structure and phase identification of the MoS_2/C samples were studied by X-ray diffraction using a Bruker D8 Advanced diffractometer (Rigaku, Tokyo, Japan) with CuKα radiation (λ = 1.54178 Å) generated at 40 kV and 200 mA. Data was collected for the 2θ range of 5 to 70 degrees, with a step of 0.0194 degree on continuous scanning mode. The morphology and structure features of MoS_2/C NCs were obtained on a JEOL JEM-2010 high-resolution

transmission electron microscope (HR-TEM, JEOL Ltd., Tokyo, Japan) at an acceleration voltage of 200 kV. Chemical composition and elemental mapping were analyzed using scanning transmission electron microscopy (S-TEM, JEM-ARM200F, JEOL Ltd., Japan) operating at 200 kV equipped with energy-dispersive X-ray spectroscopy (EDS JED-2300, JEOL, Japan). Field emission scanning electron microscopy (FE-SEM, Hitachi S-4800, Japan) at an acceleration voltage of 10 kV, was used to investigate the morphology of GO and the MoS_2/C samples. The Fourier transform infrared (FTIR) spectroscopy (Perkin Elmer Spectrum, USA) was applied to confirm the appearance of functional groups on the surface of the samples. The spectra were recorded ranging from 400 cm^{-1} to 4000 cm^{-1}. Raman spectra were carried out in frequency range of 100–3000 cm^{-1} using a Micro Raman Horiba XploRA One instrument equipped with a green Argon laser (λ = 532 nm) as the excitation source. The surface composition and chemical states of the GO and MoS_2/C samples were analysed by X-ray photoelectron spectroscopy (XPS, VG Multilab ESCA 2000 system, UK) with Al Kα X-ray ($h\nu$ = 1486.6 eV) as the source of radiation. Analysis of the XPS spectra was carried out with XPSPEAK41 software using the Gaussian−Lorentzian sum function after a Shirley background subtraction.

2.3.2. Electrode fabrication and electrochemial measurements

Cyclic voltammetry (CV) and Electrochemical impedance spectroscopy (EIS) measurements were conducted at room temperature using an electrochemical workstation PGSTAT302N (Metrohm, Switzerland) run by the NOVA v.2.1.3 software. A three-electrode electrochemical system was employed, which included a working electrode (WE) coated with MoS_2/C NC (~91.0 wt.%) and carbon black (~6.0 wt.%) on a 6-mm diameter glassy carbon electrode surface (CH Instruments, TX, USA), an Ag/AgCl (3 M KCl) reference electrode (RE), and a Pt auxiliary electrode (CE). All chemicals used in the electrochemical measurements were purchased from Sigma-Aldrich (St. Louis, MO, USA). For CV measurements, 1 M Na_2SO_4 solution was used as a buffer solution. The CV measurement were performed in the potential windows of −1.2 to 0.2 V at different scan rates in range of 5–100 mV s^{-1}. The specific capacitance (C_{sp}) of the fabricated MoS_2/C NC electrodes can be evaluated by Eq. (1) or Eq. (2):

$$C_{sp} = \frac{|Q_A| + |Q_C|}{2m \times \Delta V}, \text{ F g}^{-1} \quad (1)$$

where $|Q_A|$ and $|Q_C|$ are the charges storage at the anode and cathode, respectively, m (g) is the mass of the electrode materials, and ΔV (V) is the potential window of the CV curve. The energy density E (Wh kg^{-1}) and power density P (W kg^{-1}), were determined from the CV curve according to Eqs. (3) and (4) in which v (mV s^{-1}) is the scan rate,

$$C_{sp} = \frac{Q}{2V} = \frac{1}{2V\nu}\int_{V^-}^{V^+} i(V)dV, \text{ F g}^{-1} \quad (2)$$

$$E = \frac{1}{2}C_{sp}(\Delta V)^2, \text{ Wh kg}^{-1} \quad (3)$$

$$P = \frac{1}{2}C_{sp}(\Delta V)\nu, \text{ W kg}^{-1} \quad (4)$$

The EIS data were collected from 99 kHz to 0.01 Hz at open-circuit potential (OCP) with a voltage signal of 10 mV amplitude. The impedance measurements were carried out in 5 mM ferro/ferricyanide in 0.1 M KCl solution. DI water (Milli-Q water, 18 MΩ, Millipore Corp.,

Bilerica, MA, USA) was used for all cleaning and solution preparations. The electrode capacitance $C(\omega)$ is composed of real part $C'(\omega)$ (Eq. (5)) and the imaginary part $C''(\omega)$ (Eq. (6)) components.

$$C'(\omega) = \frac{-Z''(\omega)}{\omega|Z(\omega)|^2} \quad (5)$$

$$C''(\omega) = \frac{Z'(\omega)}{\omega|Z(\omega)|^2} \quad (6)$$

Electrochemical surface of the electrode material can be calculated by the formula (7) in which C_d is constant value of 20 μF cm^{-2} [16] and C_{dm} is calculated by Eq. (8), where Z'' is the imaginary part of impedance value calculated at responded frequency $f \sim 0.01$ Hz, and m (g) is the mass of the electrode materials.

$$S_E = \frac{C_{dm}}{C_d}, \text{ m}^2\text{ g}^{-1} \quad (7)$$

$$C_{dm} = \frac{1}{2m\pi fZ''}, \text{ F g}^{-1} \quad (8)$$

$$\tau_o = \frac{1}{2\pi f_o}, \text{ s} \quad (9)$$

The relaxation time constant τ_o (s) is defined as the minimum time needed to discharge the entire energy stored in the device with an efficiency over 50 % [17] and calculated by Eq. (9) with f_o is the knee frequency at which the imaginary component of the impedance reaches the highest value in the HF region [18].

3. RESULTS AND DISCUSSION

3.1. Structures, morphologies, chemical compositions of GO and MoS_2/C NC

The surface morphology and structural characteristics of the as-synthesized GO nanosheets have been evaluated by FE-SEM and TEM. As seen in Figure 1(a), the FE-SEM image indicates that the GO material has a layered morphology and composes of individual of GO nanosheets loosely linked with each other producing a three-dimensional network structure. From Figure 1(b), it is obvious that single and/or few GO nanosheets with typical wrinkle characteristics are produced after ultrasonication process. The edges of GO nanosheets slightly curved because of surface tension and/or the presence of oxygen-containing functional groups on its surfaces and edges. A paper-like morphology of very thin GO nanosheets was observed in TEM (Figure 1(c)). Transparent sheets of GO with the typical wrinkled and crumpled features were observed. The TEM image showed GO nanosheets with lateral dimensions in the range of a few to tens of micrometers. Thus, we had successfully synthesized GO nanosheets by chemical oxidation of graphite flakes.

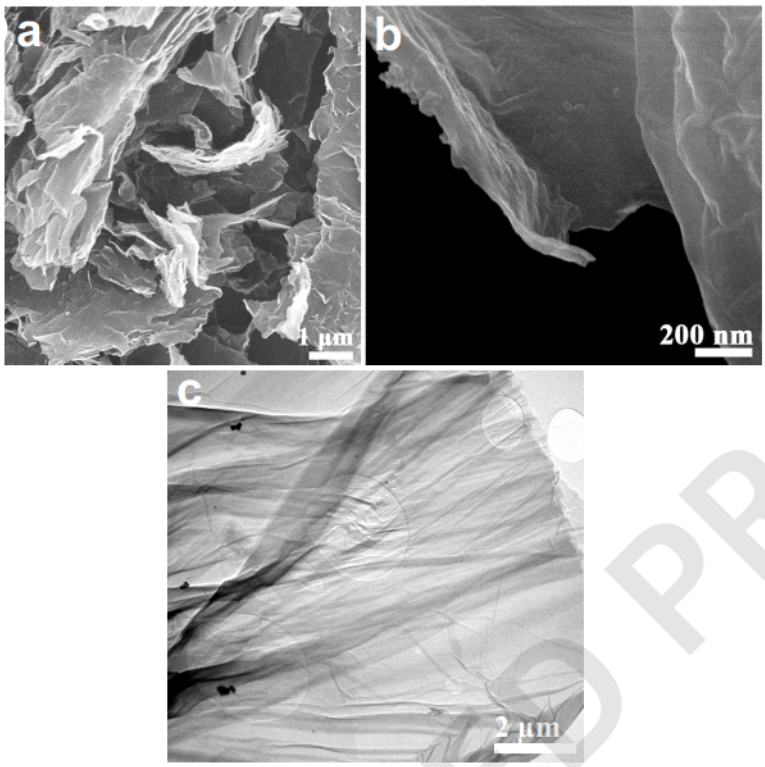

Figure 1. FESEM images at (a) low and (b) high magnification and (c) TEM image of as-prepared GO nanosheets.

The crystalline structures of the synthesized MoS_2/C NC, GO, and bare-MoS_2 samples were examined by XRD, as shown in Figure 2(a). The XRD pattern of GO shows two noticeable peaks at 2θ ~10.6° and 23.4° corresponding to (001) and (002) crystal planes, respectively. These peaks match well with those of the standard XRD pattern for GO (JCPDS #00-065-1528), confirming the successful synthesis of GO. For the MoS_2/C NC sample, the resulting XRD pattern shows diffraction peaks centered at 2θ ~14.3°, 33.1°, 40.1°, 49.3°, and 59.1°, corresponding to the (002), (100), (103), (105) and (110) crystal planes of MoS_2, respectively. These peaks match with those of the standard XRD pattern for 2H-MoS_2 (JCPDS #00-037-1492) and those of the bare-MoS_2 sample, as reported in earlier studies [14, 15, 29-31], confirming the successful synthesis of MoS_2/C NC. No other peak was detected in the patterns, demonstrating the high purity of the as-prepared samples. It can be noticed that the strong diffraction peak centered at 2θ ~14.3° of the (002) plane corresponds to the lattice plane distance $d_{(002)}$ ~0.63 nm (calculated using Bragg's equation [32]), which represents interlayer spacing of a stacked MoS_2 structure [32-34], indicating that 2D-MoS_2 crystals grew on the surfaces of GO sheets along the preferred direction of [001], as found in the literature [35, 36]. Compared to the initial GO pattern, two diffraction peaks at 2θ of ~10.6° and 23.4° almost disappeared in the XRD pattern of the MoS_2/C NC which demonstrates that the GO was successfully converted to reduced graphene oxide (rGO) during the synthesis process [37]. However, the typical diffraction peak of rGO located at ~25.4–26.8° was not detected, which could be attributed to either the low rGO concentration or the relatively low degree of crystallinity of rGO in comparison to the MoS_2 crystals. This occurred due to the existence of MoS_2 crystals onto the rGO surface, resulting in the disordered stacking of the rGO sheets inside the composite. The similar result had been observed in Refs. [32, 38, 39]. On the basis of XRD analysis, one could be concluded that the appropriate reaction temperature and

reaction time for the growth of 2D-MoS_2 nanostructures on rGO were 230 °C and 2 h, respectively [40].

The formation mechanism of 2D-MoS_2 nanostructures in-situ on GO in the hydrothermal approach can be described as the reduction of MoO_4^{2-} ions by HS^- ions to form MoS_3 according to Eq. (10) to Eq. (13), followed by the phase transition of MoS_3 to MoS_2 as described by Eq. (14).

$$(NH_4)_6Mo_7O_{24}.4H_2O \rightarrow MoO_4^{2-} + NH_3 + H_2O \quad (10)$$

$$CH_3CSNH_2\ (s) + 2H_2O \rightarrow CH_3COO^- + 2H^+ + NH_4^+ + HS^- \quad (11)$$

$$MoO_4^{2-} + 4HS^- \rightarrow MoS_4^{2-} + 4OH^- \quad (12)$$

$$MoS_4^{2-} + H^+ \rightarrow MoS_3 + HS^- \quad (13)$$

$$MoS_3 \rightarrow MoS_2 + S \quad (14)$$

Raman spectroscopy was further used to examine and validate structural and electronic properties of carbon materials [41, 42], as well as the crystal structure of MoS_2 [43, 44]. Figure 2(b) shows the Raman spectra of MoS_2, GO and MoS_2/C samples. In the Raman spectra of GO, two noticeable bands may be observed. The G-band, at ~1590.5 cm^{-1} cm^{-1}, corresponds to the presence of the sp^2-hybridization of carbon atoms and is attributed to E_{2g}-symmetry phonons of carbon atoms with sp^2-hybridization [41, 42]. The D-band, at ~1346.4 cm^{-1}, is ascribed to the K point of A_{1g}-symmetry phonons and linked to the existence of sp^3 defects and/or disordered carbon. The Raman spectrum of pure MoS_2 crystal exhibits several bands in frequency range of ~100−550 cm^{-1}. The two intensive peaks centered at ~379.1 and ~404.1 are attributed to the E^1_{2g}, and A_{1g} modes in MoS_2, respectively [44]. In addition, a small peak is observed at ~460.3 cm^{-1}, labeled as 2LA(M), which is a second-order Raman mode due to longitudinal acoustic phonons at the M point (LA(M)) in the Brillouin zone [45]. These modes correspond exactly to the characteristic structure of the semiconducting 2H-MoS_2 phase. It is the most stable phase of MoS_2 at normal conditions. Generally, the E^1_{2g} mode is associated with the in-plane vibration of Mo and S in the opposite direction, wherein the A_{1g} mode is attributed to the out-of-plane vibration of only S atoms in the opposite direction [46], as shown in the insets of Figure 2(b). The frequency variations of A_{1g} and E^1_{2g} ($\Delta\omega$) are commonly used to determine the number of layers [46]. In our study, $\Delta\omega$ is approximately 25 cm^{-1}, which is bigger than that in single-layer MoS_2 sheets (~18–19 cm^{-1}) [45, 47], but less than the average value in bulk MoS_2 (~26 cm^{-1}) [48-50]. This confirms the presence of a few layers in grown MoS_2 [51]. In the synthesized nanocomposite, apart from peaks at ~380.2, ~403.6 and ~495.0 cm^{-1} correspond to E^1_{2g}, A_{1g} and 2LA(M) modes of 2H-MoS_2, respectively; the small peak at ~230 cm^{-1} is a defect peak, which is attributed to the longitudinal (LA(M)) acoustic mode located at the M point of the Brillouin zone [45, 52]. The peak around ~520 cm^{-1} is due to the Si mode. Interestingly, the calculated intensity ratio (I_D/I_G) of D and G bands is ~0.13 for the MoS_2/C NC, which is much lower than that of GO (I_D/I_G ~1.55), implying that the in-situ growth of 2D-MoS_2 nanocrystals on GO nanosheets in hydrothermal process might reduce a significant number of structural defects and/or restore the sp^2-hybridized carbon atoms in GO nanosheets.

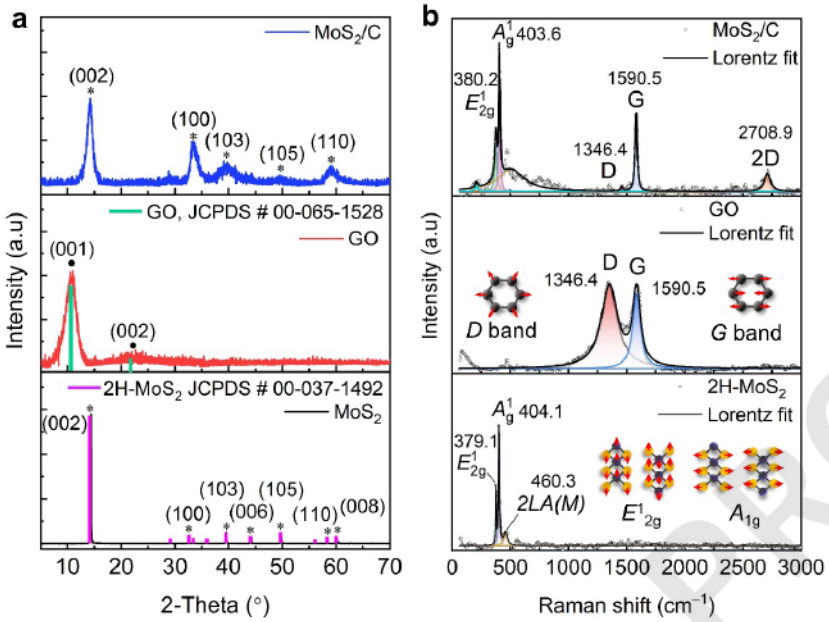

Figure 2. (a) XRD patterns and (b) Raman spectra of GO, 2D-MoS_2 and MoS_2/C NC.

FTIR spectroscopy is an extremely useful tool for identifying different functional groups contained in a sample. Accordingly, FTIR analysis is employed to elucidate the functional groups of GO, MoS_2 and the MoS_2/C NC samples. As shown in Figure 3, the absorbed peaks in range of ~3402–3200 cm^{-1} can be attributed to the –OH bending vibration from the adsorbed H_2O molecules on the surfaces of GO, 2D-MoS_2 and MoS_2/C NC. The peaks located at ~1708 and ~1390 and ~1108 cm^{-1} are due to the C=O stretching vibration of the carbonyl group [53], –OH deformations of C–OH group [61] and C–O–C stretching vibration of epoxide group [21, 54], respectively, existed in the GO nanosheets. As a result, those polar functional groups can provide anchoring sites for the adsorption of MoS_2 on the GO. The characteristic absorption peak at around ~1595–1630 cm^{-1} is attributable to the C=C skeletal vibrations from the unoxidized graphitic domains, confirming the presence of sp^2-hybridized carbon network in the GO nanosheets and MoS_2/C NC [55]. The sharp peak located at ~1406 cm^{-1} is ascribed to the stretching vibration of S–Mo–S [56]. The band centered at ~1120 cm^{-1} is related to the stretching vibration of S–O in MoS_2 nanocrystals [57]. Compared with the pristine 2D-MoS_2, a new peak appeared at ~1020 cm^{-1} in the spectrum of MoS_2/C NC which might be due to the C=S stretching mode [58], this result suggests the formation of the 2D-MoS_2 phase in the GO matrix. It was reported that interaction between C and S, most likely unsaturated S on the edges of the 2D-MoS_2 rather than the saturated S in the planes of the MoS_2, inducing that 2D-MoS_2 nanocrystals vertically grown on the GO basal plane [59, 60]. The additional peaks at ~910 and ~722 cm^{-1} are assigned to the asymmetric stretching vibration of Mo=O [61] and asymmetric vibration of the Mo–O groups [62], respectively. A peak at ~667 cm^{-1} is due to characteristic of bending vibration of S_xO_y species [63] and/or can be attributed to the S–H stretching vibrations originating as a result of dissociative H_2 adsorption on MoS_2 [64]. In contrast with the GO, the absence of the C=O and C–O–C peaks in the spectrum of MoS_2/C NC suggested that a significant amount of GO was converted to rGO during the hydrothermal process. This observation is in good agreement with the XRD analysis, in which the diffraction peaks for GO matrix disappeared in the XRD pattern of MoS_2/C NC. Combined with the Raman measurements, it was possible to conclude that the MoS_2/C nanocomposites were successfully synthesized.

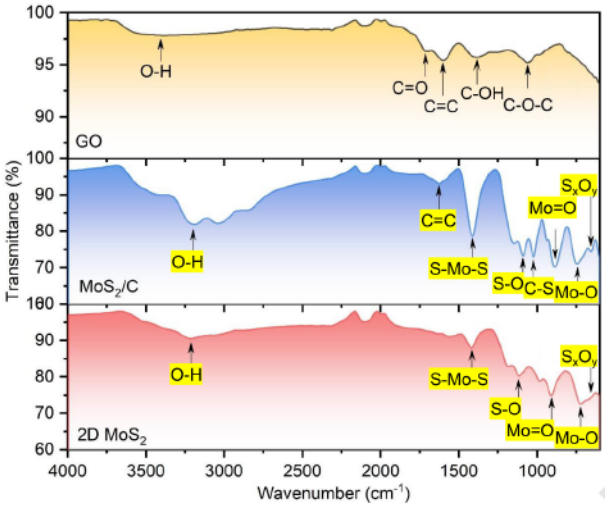

Figure 3. FTIR spectra of GO, 2D-MoS_2, and MoS_2/C NC.

The surface morphologies and architecture of the synthesized MoS_2/C NC sample can be observed as the composing of ultra-thin 2D-MoS_2 petal-liked sheets (Figure 4(a)) distributing on micron-size rGO sheets, with thickness of ~1.8–3.5 nm (~3–6 monolayers) as seen in Figures 4(d) and 4(e). The average lateral sizes of the 2D-MoS_2 petals varies from ~200 to 300 nm (Figure 4(b)). The 3D reconstructed architecture of MoS_2/C NC system in which, the formation of 2D-MoS_2 crystals on the surfaces and edges of GO nanosheets is depicted in Figure 4(f). The distinct morphological difference highlights the important role of GO matrix as an oriented platform in mediating the in-situ growth of 2D-MoS_2 nanocrystalline structures. The unique layered structure of 2D petal-liked MoS_2 crystals is easily distinguishable from the readily visible rGO sheets. These types of morphology were also observed in previously reports [22, 23]. As seen in Figure 4(f), distances between MoS_2 monolayers varies from ~0.63 to 0.86 nm obtained by measuring the extracted surface profile along the yellow dash line in Figure 4(d) and can be assigned to the (002) crystal planes of 2H-MoS_2 phase. The large $d_{(002)}$ spacing MoS_2 crystalline phase indicating that the interlayer of 2D-MoS_2 nanopetal-like sheets are significantly expanded compared to the reported for bulk value of 0.615 nm [24]. The formation of 3D architecture of MoS_2/C NC could be explained by considering the graphene self-assembling tendency, the partial overlapping or coalescing during the hydrothermal process, in which GO was reduced to rGO as evidenced by the appearance of 2D band in Raman spectrum in Figure 2(b). The above-mentioned insight analysis shows that the MoS_2/C NC system occupied a vast porous hierarchical and 3D interpenetrating structure, resulting in a large surface area and high electrical conductivity. These structural and morphological characteristics, as well as electrical capabilities, may make the produced MoS_2/C NC serve as an appealing electrode material for supercapacitors.

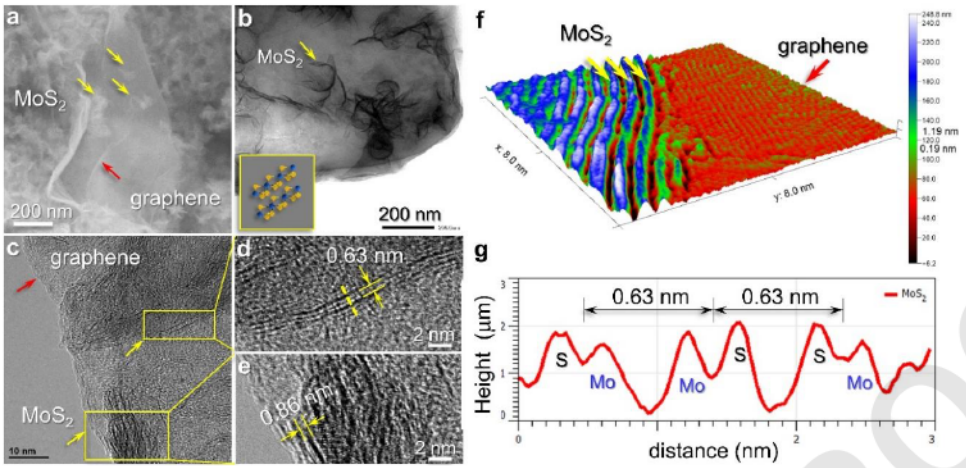

Figure 4. FE-SEM (a), TEM (b), HR-TEM (c, d, e) images; structural model of the synthesized MoS_2/C NC (f), and (g) extracted surface profile along the yellow dashed line on the HRTEM image (d).

Figure 5(a) shows a typical high-angle annular dark-field imaging scanning transmission electron microscopy (HAADF-STEM) and the corresponding EDS elemental mapping images of MoS_2/C sample (Figures 5(b)-(d)). The STEM images and EDS maps clearly present that the MoS_2 on rGO surface are very uniform and do not affect the initial morphology of the GO sheets. The EDS spectrum of the MoS_2/C in figure 5e exhibits high intensity peaks located at dispersive energy of ~0.277, ~2.293 and ~2.307 keV which correspond to the X-ray energy of C-Kα, Mo-Kα and S-Kα, reveals the presence of C, Mo, and S in the as-synthesized MoS_2/C NC sample. The elemental composition of MoS_2/C is summarized in the Table in the figure 5e, where the (Mo: C) atomic ratio is ~(1.3 : 1) and the (Mo : S) is ~(0.55 : 1). The calculated atomic ratio (Mo: C) of the synthesized MoS_2/C NC is slightly different from the designed ratio of (1.5 : 1) while the atomic ratio (Mo: S ~1: 2) is close to the molecular formula of MoS_2. Thus, the EDS results further support the FESEM, TEM/HR-TEM and Raman data, confirming the successful preparation of the nanocomposite samples by a facile hydrothermal method.

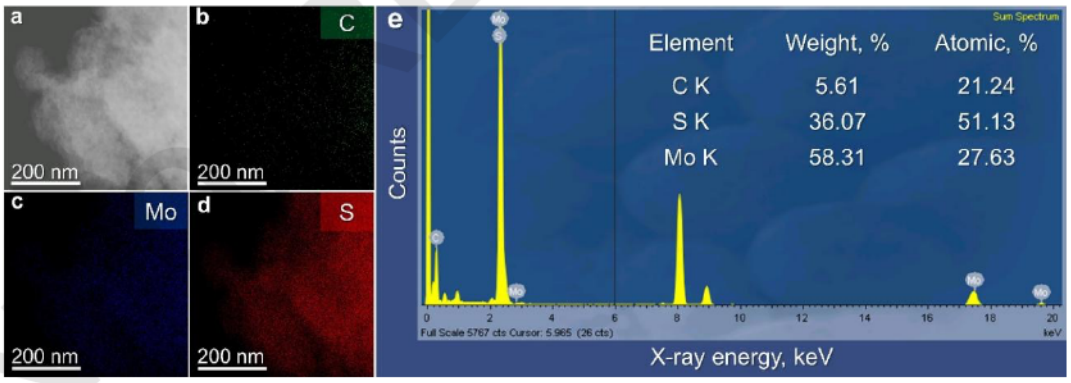

Figure 5. High-angle annular dark-field imaging (HAADF)-scanning transmission electron microscopy (STEM) and energy dispersive X-ray spectroscopy (EDS) elemental mapping images of the MoS_2/C sample: (a) HAADF-STEM image, (b) C, (c) Mo, and (d) S. (e) The EDS spectrum showing the elements and composition present in MoS_2/C NC.

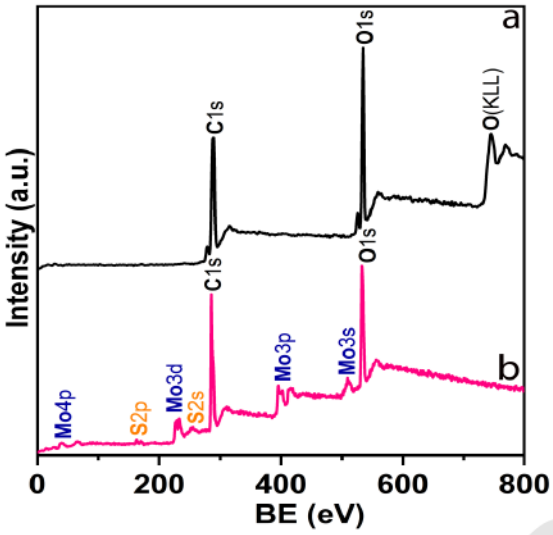

Figure 6. Raw-scan XPS spectra of (a) the as-prepared GO and (b) MoS_2/C NC.

To evaluate the surface chemical compositions and valence states of the as-prepared GO and MoS_2/C, XPS investigation was performed on the samples. C1s peak position at 284.7 eV is used as a binding energy (BE) reference to correct the XPS spectra due to any charging effect. Figures 6(a) and 6(b) show the raw-scan XPS spectra of GO and MoS_2/C samples, respectively. In the survey scan XPS spectrum of GO (Figure 6(a)), the two peaks at around ~284.7 and ~532.5 eV correspond to the C1s and O1s core level, respectively, indicating that the carbon and oxygen are the major elements in GO sheets. As for the MoS_2/C samples, four photoelectron peaks at around ~161.7, ~230.5, ~285.6 and ~533.2 eV corresponding to the S 2p, Mo 3d, C 1s and O 1s core-level, respectively, were recorded. Here, the peaks for S and Mo are expected to be from the MoS_2 material, whereas the C and O peaks are due to the presence of GO nanosheets in the samples. These results confirm that MoS_2/C NCs have been prepared successfully via a facile hydrothermal way. No other peaks related to impurities were detected in the spectra, which proved that the synthesized products were of high purity. A more detailed analysis of the chemical states of S 2p, Mo 3d, C 1s and O 1s was carried out using the narrow-scan of core level XPS spectra.

Figures 7(a)-(b) indicate the narrow-scan XPS spectra of C 1s and O 1s regions of synthesized GO sample, respectively. All XPS spectra were fixed using the mixed Gaussian-Lorentzian shape lines after Shirley baseline subtraction. As shown in Figure 7(a), the typical narrow-scan XPS spectrum of C 1s, which can be fitted into six different states. The peaks located at ~284.7, ~285.7, ~286.1, ~288.3, ~288.9 eV and ~290.4 eV, are attributed to functional groups: C=C/C-C, C-OH, C-O-C, C=O, COOH and π-π*, respectively [65]. Figure 7(b) shows the detailed fundamental line of O 1s, which can be decomposed in four signals. The two main signals are located at ~532.4 and ~533.9 eV which correspond to C-O-C and C-O bonds; whereas two weak signals appear at ~531.1 and ~535.6 eV that represent C=O and C-OH bonds, respectively.

Figures 7(c)-(f) show the typical narrow-scan XPS spectra of C 1s, S 2p, Mo 3d and O 1s regions of synthesized MoS_2/C sample, respectively. As seen in Figure 7(c), the narrow-scan XPS spectrum of C 1s, which may be classified into six sub-peaks. The peaks appeared at ~285.0, ~285.7, ~286.5, ~288.1, ~288.8 eV and ~290.0 eV, are due to functional groups: C=C/C-C, C-OH, C-O-C, C=O, COOH and π-π*, respectively. This result implies that certain functional groups are still present on the surface of GO, indicating that it was not completely eliminated.

The narrow-scan XPS spectra of O 1s in Figure 7(d) shows six unique peaks at ~531.0, ~532.3, ~533.4, ~534.7, ~536.0, and ~537.2 eV. These peaks are ascribed to C=O, C-O-C, C-O, Mo-O/S-O in MoS_xO_y due to the mild oxidation of MoS_2 exposed in air [66, 67], C-OH bonds, and H_2O, respectively. The narrow-scan XPS spectrum of S 2p can be divided into six peaks, as shown in Figure 7(e). The peaks at ~161.5 and ~163.4 eV are assigned to S^{2-} $p_{3/2}$ and S^{2-} $p_{1/2}$ in metallic 1T-MoS_2, respectively [68]. Doublet peaks at ~162.5 and ~164.7 eV are attributed to S^{2-} $p_{3/2}$ and S^{2-} $p_{1/2}$ in semiconducting 2H-MoS_2, respectively [69, 70]. Minor peaks at ~168.7 and ~169.8 eV are associated with oxidized sulfur species, including sulfate, sulfurous, and/or thiosulfate groups [71]. The narrow-scan XPS spectrum of Mo 3d was divided into seven sub-peaks centered at ~226.5, ~228.7, ~229.8, ~231.8, ~232.8, ~234.8 and ~236.9 eV, as seen in Figure 7(f). A significant peak at ~226.5 eV, which is related to S 2s [72]. The doublet peaks at ~229.8 and ~232.8 eV are ascribed to Mo^{4+} $3d_{5/2}$ and Mo^{4+} $3d_{3/2}$ in the semiconducting 2H-MoS_2 [73], whereas another two peaks at ~228.7 and ~231.8 eV with the lower binding energy by ~1.0 eV are attributed to Mo^{4+} $3d_{5/2}$ and Mo^{4+} $3d_{3/2}$ in the metallic 1T-MoS_2 [74]. The last two peaks at ~234.8 and ~236.9 eV are probably associated with the Mo^{+6} $3d_{5/2}$ [75] and Mo^{+6} $3d_{3/2}$ of MoS_xO_y [76], due to the modest surface oxidation of MoS_2 as exposed to air after the synthesis and washing, before being moved to the XPS chamber.

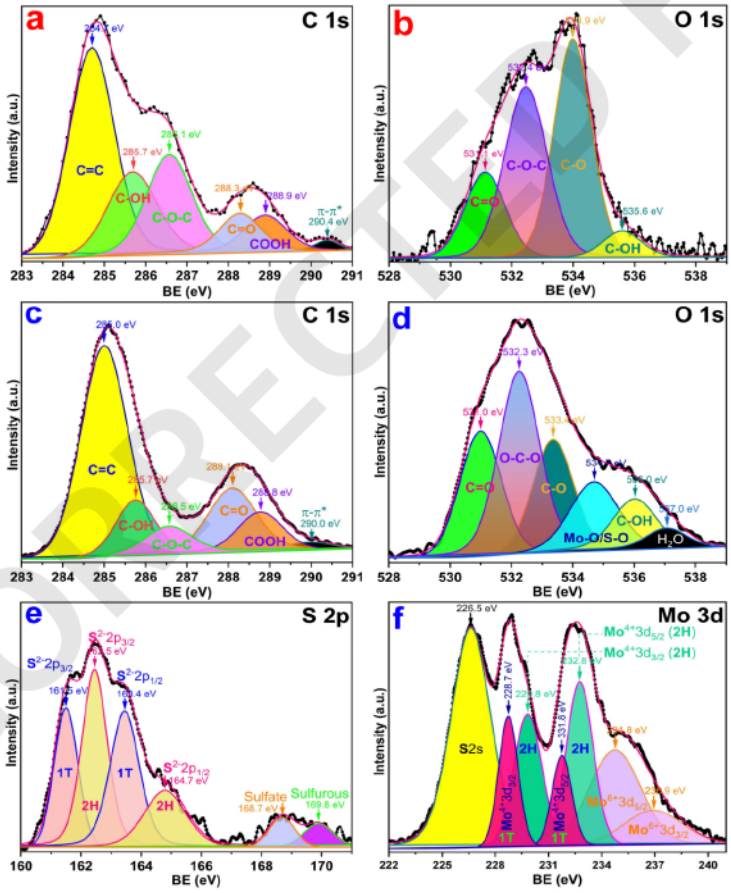

Figure 7. Narrow-scan XPS spectra of GO for (a) C 1s and (b) O 1s regions; narrow-scan XPS spectra of MoS_2/C NC for (c) C 1s and (d) O 1s, (e) S 2p and (f) Mo 3d regions.

3.2. Specific capacitance and electrochemical properties of MoS_2/C NC

The electrochemical properties of the synthesized MoS_2/C NC were investigated by CV and EIS methods, employing a three-electrode system and 3M KCl as the electrolyte. The working electrodes (GO, 2D-MoS_2 and MoS_2/C NC materials) were fabricated by coated with ~0.1 mg paste of MoS_2/C NC (93 % MoS_2/C NC and 6.0% black carbon), GO and bare 2D-MoS2, respectively. The CV curves of the electrodes fabricated were recorded at scan rates of 5–100 mV s^{-1} and shown in Figure 8. Observing the CV curve of MoS_2/C NC electrode and areas under the curves in Figure 8(a), it is clear to see that the MoS_2/C NC electrode exhibits higher specific capacitance (C_{sp}) than those of prepared GO and 2D-MoS2 electrodes. Noteworthily, the CV curve of the MoS_2/C NC approaches a rectangular-type shape of an ideal capacitor within the operating potential window between −1.1 and 0.1 V (vs. Ag/AgCl). Specifically, the MoS_2/C NC working electrode has specific capacitance of ~118.3 F g^{-1} at the scan rate of 30 mV s^{-1}, which is more 390 times higher than GO coated electrode (~0.3 F g^{-1}) and 23 times higher than 2D-MoS_2 electrode (~5.3 F g^{-1}). Furthermore, the fabricated MoS_2/C NC electrode shows improved energy density which approaching E ~87.98 Wh kg^{-1} and P ~366.6 W kg^{-1}, respectively.

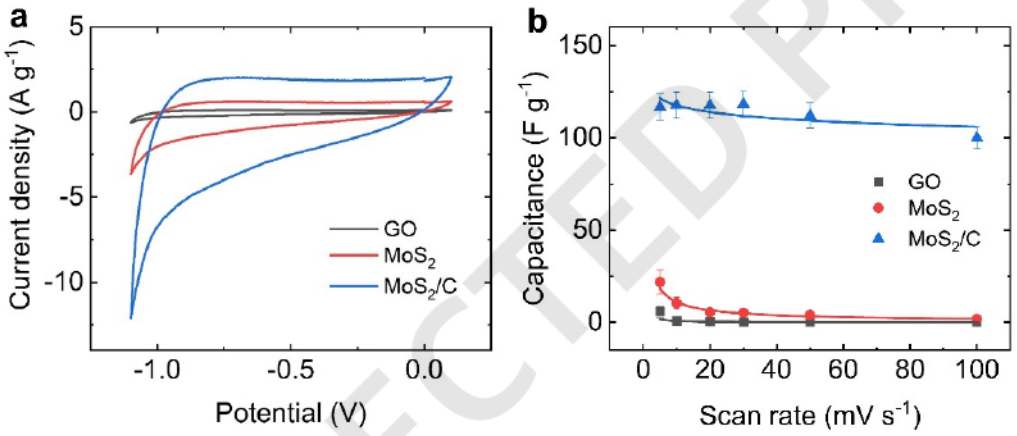

Figure 8. CV curves (a) and specific capacitances (b) of the fabricated GO, 2D-MoS2 and MoS_2/C NC electrodes.

The improved specific capacitance and energy density of MoS_2/C NC when compare to that of GO and 2D-MoS2 resulting from the its unique robust composite architecture that can be explained by two key factors: i) the rich porous 3D architecture (Figure 4) formed by growing 2D-MoS_2 crystals on the surfaces and edges of the graphene sheets. From the XRD analysis, the $d_{(002)}$ of the (002) interlayer 2D-MoS_2 structure calculated from Bragg equation is ~0.63 nm which is beneficial for rapid intercalation of hydrated $(H_2O)_6Na^+$ ions (radius of ~2.43 Å) [77]) into 2D-MoS_2 layers. This porous 3D architecture of the synthesized MoS_2/C NC allows such charged carriers as electrons and positive ions from the electrolyte to transport and diffuse more easily along the shortest routes to the electrode-electrolyte interface during the charge and discharge processes. (ii) The graphene matrix in the synthesized MoS_2/C NC system provide not only a suitable substrate for growing and dispersing 2D-MoS_2 nanocrystalline structures, whereby, increasing the specific surface area of the synthesized MoS_2/C NC, but also a highly conducting platform for fast transport of charge carriers. Specific capacitance and electrochemical performance of the capacitor electrodes fabricated from MoS_2/C NC, GO, and 2D-MoS_2 were calculated as a function of scan rate and presented in Table 1 and Table 2.

Table 1. Specific capacitance of MoS_2/C, GO, and 2D-MoS_2 electrodes.

Scan rate, mV s^{-1}	Specific capacitance, F g^{-1}		
	GO	MoS_2/C	2D-MoS_2
5	5.8	116.7	21.9
10	0.8	117.7	10.4
20	0.4	117.7	5.5
30	0.3	118.5	5.3
50	0.2	112.1	4.0
100	0.1	100.0	1.9

Table 2. Electrochemical performance of MoS_2/C, GO, and 2D-MoS_2 electrodes at the scan rate of 30 mV s^{-1}.

Electrode(s)	Potential window, V	C_{sp}, F g^{-1}	E, Wh kg^{-1}	P, W kg^{-1}
MoS_2/C	1.2	118.5	88.0	367.0
GO	1.2	0.3	0.6	0.009
2D-MoS2	1.2	5.3	10.6	0.155

As seen in Table 3, when comparing with the reported specific capacitance of MoS_2 @ 3D porous graphene (~63.8 F g^{-1}) obtained by Zhang *et al.* [78], or MoS_2 nanospheres (~112 F g^{-1}) synthesized by Kumar *et al.* [23], the specific capacitance of the as-synthesized MoS_2/C NC in this work is quite high (~118.5 F g^{-1}) over operating potential window (~ 0 ÷ -1.2 V). Our findings are mostly comparable to the previous reports [25-27], for a variety of similar composite electrode materials, demonstrating the remarkable capacitive behavior of the synthesized MoS_2/C NC [79]. These results suggest that the hydrothermal method employed in this work is more effective for synthesizing MoS_2/C NC with short reaction time and the ability to control crystalline size and morphology of the synthesized MoS_2/C NC as well as their high specific capacitance and excellent electrochemical properties.

Table 3. Comparison of specific capacitance with reported literatures.

Aqueous electrolyte	Electrode material	Device configuration	Voltage V	C_{sp} F g^{-1}	E_{sp} Wh kg^{-1}	P_{max} W kg^{-1}	Ref.
1 M Na_2SO_4	MoS_2/C NC	3-Electrode	-1.2	118.5	88.0	367.0	This work
1 M KCl	MoS_2 nanospheres	3-Electrode	-0.9	112.0	-	-	[28]
1 M $LiPF_6$	MoS_2 @ 3D porous graphene	2-Electrode	4.0	63.8	97	8314	[78]
1 M Na_2SO_4	MoS_2/C nanosheets	3-Electrode	-0.6	108.0	7.40	3700	[25]
0.1 M Na_2SO_4	RGO	3-Electrode	-0.8	41.0	-	-	[26]
3 M KOH	C/MoS_2	3-Electrode	0.5	210.0	-	-	[27]

Electrochemical impedance spectroscopy (EIS) is an important technique that widely employed to analyze the material structure and kinetics processes occurred at the electrode-electrolyte interface, whereby, providing the insight to the underlying charged storage mechanism

in MoS_2/C NC electrode system. The impedance measurements were conducted on the fabricated MoS_2/C NC, GO, and 2D-MoS_2 electrodes in the frequency range of 10 mHz to 100 kHz at the open-circuit potential window from −1.2 to 0.2 V, with an alternating voltage amplitude of 10 mV (Figures 9(a)–(c), (d)). The complex impedance $Z(\omega)$ of the synthesized MoS_2/C NC were modeled and presented as Nyquist plot (Z' vs. $-Z''$), and Bode plot, in which $Z'(\omega)$ and $Z''(\omega)$ are the real and the imaginary part, respectively, of the impedance. The Nyquist plots of the synthesized GO, 2D-MoS_2 and MoS_2/C NC system Figures 9(a), (c) displayed two distinct regimes compacted with a semicircle in the high-frequency (HF) region and a linear portion in the low-frequency (LF) region. Based on the Nyquist plot data, the electrode-electrolyte interface can be modeled by an equivalent circuit (Figure 9(e)) in which the equivalent series resistance R_S (Ω cm^2) is composed of ionic resistance of the electrolyte, intrinsic resistance of MoS_2/C NC, and the contact resistance at the interface of the MoS_2/C NC electrode material and the current collector. The R_{CT} (Ω cm^2) is the faradaic charge transfer resistance, W (S s$^{-1/2}$ cm^{-2}) is the Warburg impedance associated with ionic diffusion in the electrolyte, and C_{dl} (F cm^{-2}) is the double layer capacitance.

Electrochemical fitted parameters of the electrodes fabricated from MoS_2/C NC, GO, and 2D-MoS_2 are summarized in Table 4. It is noticed that the fabricated MoS_2/C NC electrode possesses small values of resistance R_S and R_{CT} when compared with that of GO and 2D-MoS_2 electrodes. It can be seen that in the HF region, the intrinsic resistance R_{CT} of GO electrode is ~2.616 Ω cm^{-2} while the MoS_2/C NC is ~22.610 Ω cm^{-2}, which is much lower than that of 2D-MoS_2 alone (~72.550 Ω cm^{-2}), indicated by the radius of the corresponding semi-circles in Figure 9(c). The low resistance values are beneficial, and responsible for enhancement of electrical transport property such as the fast charge transfer and ions diffusion to enhance electrochemical performance of the synthesized MoS_2/C NC electrode material.

Table 4. Electrochemical parameters calculated for MoS_2/C NC, GO, and 2D-MoS_2 electrodes.

Electrode materials	R_S (Ω cm^2)	R_{CT} (Ω cm^2)	C_{dl} (mF cm^2)	W (S s$^{-1/2}$ cm^{-2})	S_E (m^2 g^{-1})	τ_o (ms)
MoS_2/C NC	25.680	22.610	23.550	0.0028	217.6	159.1
2D-MoS_2	26.170	72.550	0.752	0.0012	124.5	0.032
GO	27.310	2.616	9.086 10^{-3}	0.0016	161.7	0.025

The complex model of the capacitance was also investigated to study the relationship between the specific capacitance of the as-fabricated MoS_2/C NC electrode and applied frequency as seen in Figures 9(b) and 9(d). The Bode plots in Figures 9(b) and 9(d) show the frequency responses of the electrode materials under the applied frequency. In this model, the cell capacitance can be expressed as real and imaginary parts according to the Eqs. (5) and (6). Compared with GO and 2D-MoS_2 electrodes, the MoS_2/C NC electrode system shows a considerably low in frequency response with large phase angle ($-\phi$, °), which is a characteristic of good capacitive performance and large energy storage capability. The response frequency of MoS_2/C NC electrode (~1.0 Hz) is significantly lower than those of 2D-MoS_2 (~5012 Hz) and GO electrodes (~6309 Hz). Furthermore, the relaxation time τ (s) calculated from the knee frequency f_o, (Hz) corresponding to the maximum of $-Z''(\omega)$ in the Nyquist Plot (LF region) was used to evaluate the electrochemical capacitance properties and charge–discharge characteristic response. The τ values obtained for the MoS_2/C NC, GO and bare 2D-MoS_2 electrodes are about ~159.1, 0.025 and 0.032 ms, respectively. The relaxation time of the MoS_2/C NC electrode to be significantly higher than that of GO and bare 2D-MoS_2, indicating the low-discharge

characteristic response and good electrochemical capacitive storage. In addition, the charge conductivity of MoS_2/C NC electrode also increases significantly compared with that of 2D-MoS_2 due to the presence of graphene matrix in the MoS_2/C NC nanocomposite.

The electrochemical active surface area S_E ($m^2\ g^{-1}$) of the fabricated MoS_2/C NC electrode system can be calculated from Eq. (7) found to be ~ 218.0 $m^2\ g^{-1}$ which is high than that of GO (~161.7 $m^2\ g^{-1}$) and bare 2D-MoS_2 (~124.5 $m^2\ g^{-1}$) electrodes which are consistent with previously reports [80]. The large active surface area of the MoS_2/C NC implies that the 2D-MoS_2 nanostructure growing and well dispersing in the graphene matrix and resulting a rich porous composite architecture as previously observed by TEM and HRTEM images in Figure 4.

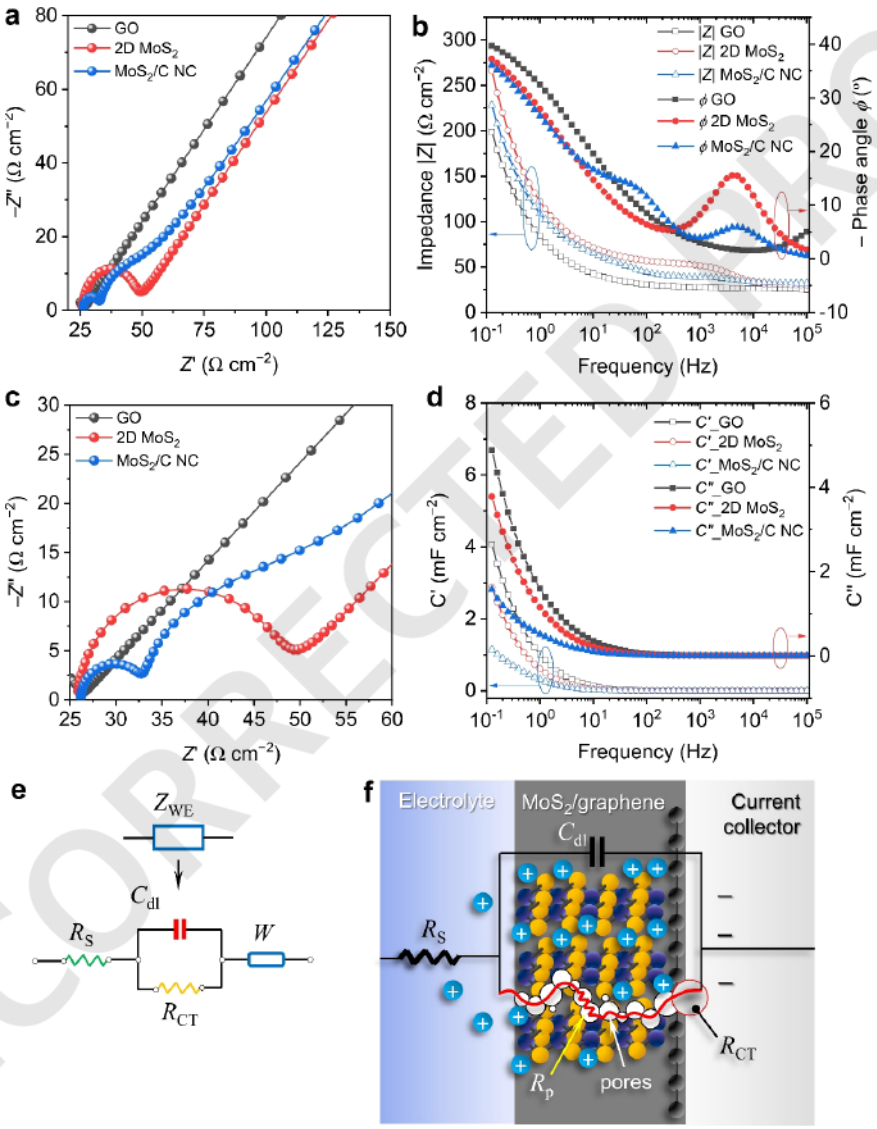

Figure 9. Electrochemical impedance of MoS_2/C NC, GO, and 2D-MoS_2 electrodes. (a) Nyquist plot, (b) Bode plot, (c) Magnified view of (a) in the high frequency region, and (d) capacitances with respect to frequencies. (e) Equivalent circuit modeling the electrolyte-electrode interface. (f) Schematic diagram showing the electric double layer and intercalation of ions between 2D-MoS_2 layers.

The capacitive energy storage mechanism of the electrode material can be described as the accumulation of charges at the electrolyte-electrode interface. The enhancement in capacitive energy storage in the case of MoS_2/C NC electrode system can be related to the combination of electric double-layer capacitive mechanism and faradic/redox mechanism and the increased electrochemical surface due to the minimized number of monolayers of MoS_2 crystals grown on the graphene sheets during the hydrothermal process. First, ions accumulate at the interface of the electric double layer between MoS_2 nanocrystalline sheets and the electrolyte as illustrated in figure 9f. Then, during charging, alkali ions from the electrolyte (Na^+ in this case) adsorb on the surfaces and intercalate between 2D-MoS_2 layers (reduction reaction), followed by discharging and deintercalation of the ions (oxidation reaction) as represented by faradaic (Eq. (15)) and non-faradaic (Eq. (16)) mechanism [81, 82]:

$$MoS_2 + yNa^+ + ye^- \leftrightarrow NayMoS_2 \quad (15)$$

$$(MoS_2)_{surface} + yNa^+ \leftrightarrow (Na^+ - MoS_2^-)_{surface} \quad (16)$$

It is evident that the electrical double-layer capacitance is contributed by the graphene matrix, whereas the pseudo-capacitance is associated with the surface redox of 2D-MoS_2 phase dispersed in the graphene matrix. The presence of graphene matrix in the MoS_2/C NC providing a high electronic conductive platform and large specific surface area for growing 2D-MoS_2 nanostructures. In addition, the intercalation of large ions from the electrolyte to the vdW gaps between MoS_2 layers prevented them from aggregation. The repeated intercalation – deintercalation of the ions and charged carriers during multiple charging/discharging process could enlarge the MoS_2 intra-layer gaps and even exfoliate 2D-MoS_2 monolayers. This process results in an increased overall specific surface area and thereby, enhance the specific capacitance of the MoS_2/C NC electrode system.

4. CONCLUSIONS

Low-dimensional MoS_2/C NC material with 3D porous morphology was successfully synthesized by in-situ growing 2D-MoS_2 crystals inside GO matrix via a simple one-pot hydrothermal approach. The morphology, phase, chemical composition, and electrochemical properties of the as-synthesized materials were studied by various characterization methods including FE-SEM, HR-TEM, XRD, EDS, XPS, FTIR, Raman spectroscopy, and electrochemical measurements. The results provided that the 2H-MoS_2 nanocrytals had a petal-like form with thickness of ~1.8-3.5 nm and average lateral size of ~200-300 nm, which were distributed on the surfaces of GO nanosheets. The electrochemical measurements indicated that the MoS_2/C NC possesses high specific capacitance of ~118.5 F g^{-1}, energy density of ~88.0 Wh kg^{-1}, and a power density of ~367.0 W kg^{-1} with large specific surface area of ~218.0 m^2 g^{-1}. The ultrathin 2D-MoS_2 nanocrystals, as well as the synergistic impact between the 2D-MoS_2 dispersion phase and the GO matrix, improved the charge storage of MoS_2/C NC, which could be responsible for the enhancement of specific capacitance and electrochemical performance of the MoS_2/C NC material. These findings suggested that the produced MoS_2/C NC could be an effective electrode material for supercapacitors in microelectronic devices.

Acknowledgments. This research is funded by Vietnam National Foundation for Science and Technology Development (NAFOSTED) under Grant No. 104.03-2019.42. We acknowledge the support of time and facilities from Ho Chi Minh City University of Technology (HCMUT), VNU-HCM for supporting this study.

CRediT authorship contribution statement. Le Ngoc Long: Investigation, Methodology, Visualization, Writing – original draft. Tran Van Khai: Conceptualization, Data curation, Formal analysis, Resources, Supervision, Validation, Writing – review & editing.

Declaration of competing interest. The authors declare that they have no known competing financial interests or personal relationships that could have appeared to influence the work reported in this paper.

REFERENCES

1. Conway B. E. - Electrochemical Supercapacitors: Scientific Fundamentals and Technological Applications. Plenum, New York (1999).
2. Miller J. R., Simon P. - Electrochemical capacitors for energy management. Science, **321**(5889) (2008) 651-652. https://doi.org/10.1126/science.1158736.
3. Geim A. K. - Nobel Lecture: Random walk to graphene. Rev. Mod. Phys., **83**(3) (2011) 851-862. https://doi.org/10.1103/RevModPhys.83.851.
4. Novoselov K. S., Geim A. K., Morozov S. V., Jiang D., Zhang Y., Dubonos S. V., Grigorieva I. V., Firsov A. A. - Electric field effect in atomically thin carbon films. Science, **306** (2004) 666-669. https://doi.org/10.1126/science.1102896.
5. Castro Neto A. H., Guinea F., Peres N. M. R., Novoselov K. S., Geim A. K. - The electronic properties of graphene. Rev. Mod. Phys., **81** (2009) 109-162. https://doi.org/10.1103/RevModPhys.81.109.
6. Abergel D. S. L., Apalkov V., Berashevich J., Ziegler K., Chakraborty T. - Properties of graphene: a theoretical perspective. Adv. Phys., **59** (2010) 261-482. https://doi.org/10.1080/00018732.2010.487978.
7. Huang K. J., Wang L., Liu Y. J., Liu Y. M., Wang H. B., Gan T., Wang L. L. - Layered MoS_2-graphene composites for supercapacitor applications with enhanced capacitive performance. Int. J. Hydrogen Energy, **38** (2013) 14027-14034. https://doi.org/10.1016/j.ijhydene.2013.08.112.
8. David L., Bhandavat R., Singh G. - MoS_2/graphene composite paper for sodium-ion battery electrodes. ACS Nano, **8** (2014) 1759-1770. https://doi.org/10.1021/nn406156b.
9. Ma L., Huang G., Chen W., Wang Z., Ye J., Li H., Chen D. N. S., Lee J. Y. - Cationic surfactant-assisted hydrothermal synthesis of few-layer molybdenum disulfide/graphene composites: microstructure and electrochemical lithium storage. J. Power Sources, **264** (2014) 262-271. https://doi.org/10.1016/j.jpowsour.2014.04.084.
10. Hu H., Zhao Z., Wan W., Gogotsi Y., Qiu J. - Ultralight and highly compressible graphene aerogels. Adv. Mater., **25** (2013) 2219-2223. https://doi.org/10.1002/adma.201204530.
11. da Silveira Firmiano E. G., Rabelo A. C., Dalmaschio C. J., Pinheiro A. N., Pereira E. C., Schreiner W. H., Leite E. R. - Supercapacitor electrodes obtained by directly bonding 2D-MoS_2 on reduced graphene oxide. Adv. Energy Mater., **4** (2014) 1301380. https://doi.org/10.1002/aenm.201301380.
12. Yang M. H., Jeong J. M., Huh Y. S., Choi B. G. - High-performance supercapacitor based on three-dimensional MoS_2/graphene aerogel composites. Compos. Sci. Technol., **121** (2015) 123-128. https://doi.org/10.1016/j.compscitech.2015.11.004.
13. Mak K. F., Lee C., Hone J., Shan J., Heinz T. F. - Atomically thin MoS_2: a new direct-gap semiconductor. Phys. Rev. Lett., **105** (2010) 136805-136808. https://doi.org/10.1103/PhysRevLett.105.136805.
14. Li X., Guo S., Li W., Ren X., Su J., Song Q., Sobrido A. J., Wei B. - Edge-rich MoS_2 grown on edge-oriented three-dimensional graphene glass for high-performance hydrogen evolution. Nano Energy, **57** (2019) 388-397. https://doi.org/10.1016/j.nanoen.2018.12.044.
15. Yadav V., Roy S., Singh P., Khan Z., Jaiswal A. - 2D MoS_2-based nanomaterials for therapeutic, bioimaging, and biosensing applications. Small, **15** (2019) 1803706. https://doi.org/10.1002/smll.201803706.
16. Zhang W., Zhang P., Su Z., Wei G. - Synthesis and sensor applications of MoS_2-based nanocomposites. Nanoscale, **7** (2015) 18364-18378. https://doi.org/10.1039/C5NR06121K.

17. Naz R., Imtiaz M., Liu Q., Yao L., Abbas W., Li T., Zada I., Yuan Y., Chen W., Gu J. - Highly defective 1T-MoS_2 nanosheets on 3D reduced graphene oxide networks for supercapacitors. Carbon, **152** (2019) 697-703. https://doi.org/10.1016/j.carbon.2019.06.009.
18. Britnell L., Ribeiro R. M., Eckmann A., Jalil R., Belle B. D., Mishchenko A., Kim Y. J., Gorbachev R. V., Georgiou T., Morozov S. V., Grigorenko A. N., Geim A. K., Casiraghi C., Castro-Neto A. H., Novoselov K. S. - Strong light-matter interactions in heterostructures of atomically thin films. Science, **340**(6138) (2013) 1311-1314. https://doi.org/10.1126/science.1235547.
19. Kuc A. - Low-dimensional transition-metal dichalcogenides. Chem. Modell., **11** (2014) 1-29. https://doi.org/10.1039/9781782620112-00001.
20. Novoselov K. S., Jiang D., Schedin F., Booth T. J., Khotkevich V. V., Morozov S. V., Geim A. K. - Two-dimensional atomic crystals. Proc. Natl. Acad. Sci. U.S.A., **102** (2005) 10451-10453. https://doi.org/10.1073/pnas.0502848102.
21. Sirat M. S., Johari M. H., Mohmad A. R., Haniff M. A. S. M., Ani M. H., Hussin M. R. M., Mohamed M. A. - Direct growth and properties of few-layer MoS_2 on multilayer graphene prepared by chemical vapor deposition. J. Mater. Sci., **57** (2022) 19704-19715. https://doi.org/10.1007/s10853-022-07873-7.
22. Shi Y., Zhou W., Lu A. Y., Fang W., Lee Y. H., Hsu A. L., Kim S. M., Kim K. K., Yang H. Y., Li L. J., Idrobo J. C., Kong J. - van der Waals epitaxy of MoS_2 layers using graphene as growth templates. Nano Lett., **12** (2012) 2784-2791. https://doi.org/10.1021/nl204562j.
23. Kumar D. P., Hong S., Reddy D. A., Kim T. K. - Ultrathin MoS_2 layers anchored exfoliated reduced graphene oxide nanosheet hybrid as a highly efficient cocatalyst for CdS nanorods towards enhanced photocatalytic hydrogen production. Appl. Catal., B, **212** (2017) 7-14. https://doi.org/10.1016/j.apcatb.2017.04.065.
24. Fu M., Zhu Z., Chen W., Yu H., Liu Q. - Microwave-assisted synthesis of MoS_2/graphene composites for supercapacitors. J. Mater. Sci., **55** (2020) 16385-16393. https://doi.org/10.1007/s10853-020-05201-5.
25. Hummers W. S., Offeman R. E. - Preparation of graphitic oxide. J. Am. Chem. Soc., **80**(6) (2002) 1339-1339. https://doi.org/10.1021/ja01539a017.
26. Khai T. V., Lam T. D., Thu L. V., Kim H. W. - A two-step method for the preparation of highly conductive graphene film and its gas-sensing property. Mater. Sci. Appl., **6** (2015) 963-977. https://doi.org/10.4236/msa.2015.611097.
27. Khai T. V., Long L. N., Khoi N. H. T., Thang N. H. - Effects of hydrothermal reaction time on the structure and optical properties of ZnO/graphene oxide nanocomposites. Crystals, **12**(12) (2022) 1825. https://doi.org/10.3390/cryst12121825.
28. Khai T. V., Kwak D. S., Kwon Y. J., Kim S. S., Shim K. B., Kim H. W. - High-quality graphene thin films synthesized by H2 ambient-annealing of reduced graphene oxide sheets. J. Ceram. Process. Res., **14** (2013) 355-362.
29. Peng X., Peng L., Wu C., Xie Y. - Two dimensional nanomaterials for flexible supercapacitors. Chem. Soc. Rev., **43** (2014) 3303-3323. https://doi.org/10.1039/c3cs60407a.
30. Long L. N., Kien P. T., Khai T. V. - Synthesis of MoS_2/graphene nanocomposite by facile ultrasonic-assisted hydrothermal method. Vietnam J. Sci. Technol., **57**(6) (2019) 703-713. https://doi.org/10.15625/2525-2518/57/6/13955.
31. Xuan T. T., Long L. N., Khai T. V. - Effect of reaction temperature and reaction time on the structure and properties of MoS_2 synthesized by hydrothermal method. Vietnam J. Chem., **58** (2020) 92-100. https://doi.org/10.1002/vjch.2019000144.
32. Long L. N., Quang N. T., Khuong T. T., Kien P. T., Thang N. H., Khai T. V. - Controllable synthesis by hydrothermal method and optical properties of 2D MoS_2/rGO nanocomposites. J. Sol-Gel Sci. Technol., **106** (2023) 699-714. https://doi.org/10.1007/s10971-023-06072-3.
33. Yunus R. M., Endo H., Tsuji M., Ago H. - Vertical heterostructures of MoS_2 and graphene nanoribbons grown by two-step chemical vapor deposition for high-gain photodetectors. Phys. Chem. Chem. Phys., **17** (2015) 25210-25215. https://doi.org/10.1039/C5CP03958D.

34. Zhao B., Wang Z., Gao Y., Chen L., Lu M., Jiao Z., Jiang Y., Ding Y., Cheng L. - Hydrothermal synthesis of layer-controlled MoS_2/graphene composite aerogels for lithium-ion battery anode materials. Appl. Surf. Sci., **390** (2016) 209-215. https://doi.org/10.1016/j.apsusc.2016.08.078.
35. Fei L., Lei S., Zhang W. B., Lu W., Lin Z., Lam C. H., Chai Y., Yu W. - Direct TEM observations of growth mechanisms of two-dimensional MoS_2 flakes. Nat. Commun., **7** (2016) 12206. https://doi.org/10.1038/ncomms12206.
36. Yang L., Cui X., Zhang J., Wang K., Shen M., Zeng S., Dayeh S. A., Feng L., Xiang B. - Lattice strain effects on the optical properties of MoS_2 nanosheets. Sci. Rep., **4** (2014) 5649. https://doi.org/10.1038/srep05649.
37. Nethravathi C., Rajamathi M. - Chemically modified graphene sheets produced by the solvothermal reduction of colloidal dispersions of graphite oxide. Carbon, **46** (2008) 1994-1998. https://doi.org/10.1016/j.carbon.2008.08.013.
38. Guo J., Chen X., Jin S., Zhang M., Liang C. - Synthesis of graphene-like MoS_2 nanowall/graphene nanosheet hybrid materials with high lithium storage performance. Catal. Today, **246** (2015) 165-171. https://doi.org/10.1016/j.cattod.2014.09.028.
39. Zou L., Qu R., Gao H., Guan X., Qi X., Liu C., Zhang Z., Lei X. - MoS_2/RGO hybrids prepared by a hydrothermal route as a highly efficient catalytic for sonocatalytic degradation of methylene blue. Results Phys., **14** (2019) 102458. https://doi.org/10.1016/j.rinp.2019.102458.
40. Long L. N., Thi P. T., Trung P. T., Kien P. T., Ohtani M., Kumabe Y., Tanaka H., Ueda S., Lee H., Thang P. B., Khai T. V. - Controllable synthesis of MoS_2/graphene low-dimensional nanocomposites and their electrical properties. Appl. Surf. Sci., **504** (2020) 144193. https://doi.org/10.1016/j.apsusc.2019.144193.
41. Bokobza L., Bruneel J. L., Couzi M. - Raman spectroscopy as a tool for the analysis of carbon-based materials (highly oriented pyrolitic graphite, multilayer graphene and multiwall carbon nanotubes) and of some of their elastomeric composites. Vib. Spectrosc., **74** (2014) 57-63. https://doi.org/10.1016/j.vibspec.2014.07.009.
42. Ferrari A. C., Basko D. M. - Raman spectroscopy as a versatile tool for studying the properties of graphene. Nat. Nanotechnol., **8** (2013) 235-246. https://doi.org/10.1038/nnano.2013.46.
43. Buscema M., Steele G. A., van der Zant H. S. J., Castellanos-Gomez A. - The effect of the substrate on the Raman and photoluminescence emission of single-layer MoS_2. Nano Res., **7** (2014) 561-571. https://doi.org/10.1007/s12274-014-0424-0.
44. Golasa K., Grzeszczyk M., Bozek R., Leszczynski P., Wysmolek A., Potemski M., Babinski A. - Resonant Raman scattering in MoS_2 - from bulk to monolayer. Solid State Commun., **197** (2014) 53-56. https://doi.org/10.1016/j.ssc.2014.08.009.
45. Mignuzzi S., Pollard A. J., Bonini N., Brennan B., Gilmore I. S., Pimenta M. A., Richards D., Roy D. - Effect of disorder on Raman scattering of single-layer MoS_2. Phys. Rev. B, **91** (2015) 195411. https://doi.org/10.1103/PhysRevB.91.195411.
46. Lee C., Yan H., Brus L. E., Heinz T. F., Hone J., Ryu S. - Anomalous lattice vibrations of single- and few-layer MoS_2. ACS Nano, **4** (2010) 2695-2700. https://doi.org/10.1021/nn1003937.
47. Molina-Sanchez A., Wirtz L. - Phonons in single-layer and few-layer MoS_2 and WS_2. Phys. Rev. B, **84** (2011) 155413. https://doi.org/10.1103/PhysRevB.84.155413.
48. Liu Y. J., Hao L. Z., Gao W., Liu Y. M., Li G. X., Xue Q. Z., Guo W. Y., Yu L. Q., Wu Z. P., Liu X. H., Zeng H. Z., Zhu J. - Growth and humidity-dependent electrical properties of bulk-like MoS_2 thin films on Si. RSC Adv., **5** (2015) 74329-74335. https://doi.org/10.1039/C5RA11454C.
49. Chakraborty B., Matte H. S. S. R., Sood A. K., Rao C. N. R. - Layer-dependent resonant Raman scattering of a few layer MoS_2. J. Raman Spectrosc., **44** (2013) 92. https://doi.org/10.1002/jrs.4147.
50. Ganatra R., Zhang Q. - Few-layer MoS_2: a promising layered semiconductor. ACS Nano, **8** (2014) 4074-4099. https://doi.org/10.1021/nn405938z.
51. Hussain S., Shehzad M. A., Vikraman D., Khan M. F., Singh J., Choi D., Seo Y., Eom J., Lee W., Jung J. - Synthesis and characterization of large-area and continuous MoS_2 atomic layers by RF magnetron sputtering. Nanoscale, **8** (2016) 4340-4347. https://doi.org/10.1039/C5NR09032F.

52. Zhang X., Qiao X., Shi W., Wu J., Jiang D., Tan P. - Phonon and Raman scattering of two-dimensional transition metal dichalcogenides from monolayer, multilayer to bulk material. Chem. Soc. Rev., **44** (2015) 2757-2785. https://doi.org/10.1039/C4CS00282B.
53. Aliyev E., Filiz V., Khan M. M., Lee Y. J., Abetz C., Abetz V. - Structural characterization of graphene oxide: surface functional groups and fractionated oxidative debris. Nanomaterials, **9**(8) (2019) 1180. https://doi.org/10.3390/nano9081180.
54. Khai T. V., Long L. N., Phong M. T., Kien P. T., Thang L. V., Lam T. D. - Synthesis and optical properties of MoS_2/graphene nanocomposite. J. Electron. Mater., **49** (2020) 969-979. https://doi.org/10.1007/s11664-019-07670-0.
55. Pang Y. L., Tee S. F., Lim S., Abdullah A. Z., Ong H. C., Wu C. H., Chong W. C., Mohammad A. W., Mahmoudi E. - Enhancement of photocatalytic degradation of organic dyes using ZnO decorated on reduced graphene oxide (rGO). Desalin. Water Treat., **108** (2018) 311-321. https://doi.org/10.5004/dwt.2018.21947.
56. Ali M. E. M., Mohammed R., Abdel Moniem S. M., El Liethy M. A., Ibrahim H. S. - Green MoS_2 nanosheets as a promising material for decontamination of hexavalent chromium, pharmaceuticals, and microbial pathogen disinfection: spectroscopic study. J. Nanopart. Res., **24** (2022) 191. https://doi.org/10.1007/s11051-022-05573-6.
57. Liu Y., Zhao Y., Jiao L., Chen J. - A graphene-like MoS_2/graphene nanocomposite as a high-performance anode for lithium ion batteries. J. Mater. Chem. A, **2** (2014) 13109-13115. https://doi.org/10.1039/C4TA01644K.
58. Wiles D. M., Gingras B. A., Suprunchuk T. - The C=S stretching vibration in the infrared spectra of some thiosemicarbazones. Can. J. Chem., **45**(5) (1967) 469-473. https://doi.org/10.1139/v67-081.
59. Deng Z. H., Li L., Ding W., Xiong K., Wei Z. D. - Synthesized ultrathin MoS_2 nanosheets perpendicular to graphene for catalysis of hydrogen evolution reaction. Chem. Commun., **51** (2015) 1893-1896. https://doi.org/10.1039/C4CC08491H.
60. Teng Y., Zhao H., Zhang Z., Li Z., Xia Q., Zhang Y., Zhao L., Du X., Du Z., Lv P., Swierczek K. - MoS_2 nanosheets vertically grown on graphene sheets for lithium ion battery anodes. ACS Nano, **10**(9) (2016) 8526-8535. https://doi.org/10.1021/acsnano.6b03683.
61. Kee C. W. - Assignment of O-O and Mo=O stretching frequencies of molybdenum/tungsten complexes revisited. J. Chem., **2015** (2015) 439270-439279. https://doi.org/10.1155/2015/439270.
62. Ritika, Kaur M., Umar A., Mehta S. K., Singh S., Kansal S. K., Fouad H., Alothman O. Y. - Rapid solar-light driven superior photocatalytic degradation of methylene blue using MoS_2-ZnO heterostructure nanorods photocatalyst. Materials, **11**(11) (2018) 2254. https://doi.org/10.3390/ma11112254.
63. Mauge F., Lamotte J., Nesterenko N. S., Manoilova O., Tsyganenko A. A. - FTIR study of surface properties of unsupported MoS_2. Catal. Today, **70**(1) (2001) 271-284. https://doi.org/10.1016/S0920-5861(01)00423-0.
64. Wright C. J., Sampson C., Fraser D., Moyes R. B., Wells P. B., Riekel C. - Hydrogen sorption by molybdenum sulphide catalysts. J. Chem. Soc., Faraday Trans. 1, **76** (1980) 1585-1598. https://doi.org/10.1039/f19807601585.
65. Ganguly A., Sharma S., Papakonstantinou P., Hamilton J. - Probing the thermal deoxygenation of graphene oxide using high-resolution in situ X-ray-based spectroscopies. J. Phys. Chem. C, **115** (2011) 17009-17019. https://doi.org/10.1021/jp203741y.
66. Gao J., Li B. C., Tan J. W., Chow P., Lu T. M., Koratkar N. - Aging of transition metal dichalcogenide monolayers. ACS Nano, **10** (2016) 2628-2635. https://doi.org/10.1021/acsnano.5b07677.
67. Lu Q., Yang Y., Feng J., Wang X. - Oxygen-defected molybdenum oxides hierarchical nanostructure constructed by atomic-level thickness nanosheets as an efficient absorber for solar steam generation. Sol. RRL, **3** (2019) 1800277. https://doi.org/10.1002/solr.201800277.
68. Li Z., Zhan X., Qi S. - A facile alkali metal hydroxide-assisted controlled and targeted synthesis of 1T MoS_2 single-crystal nanosheets for lithium ion battery anodes. Nanoscale, **11** (2019) 14857-14862. https://doi.org/10.1039/C9NR04537F.

69. Tang Y., Zhao Z., Wang Y., Dong Y., Liu Y., Wang X., Qiu J. - Ultrasmall MoS_2 nanosheets mosaiced into nitrogen-doped hierarchical porous carbon matrix for enhanced sodium storage performance. Electrochim. Acta, **225** (2017) 369-377. https://doi.org/10.1016/j.electacta.2016.12.176.
70. Wang Y., Sun S., Liu Y., Zhang Y., Xia J., Yang Q. - TiO2 coupled to predominantly metallic MoS_2 for photocatalytic degradation of rhodamine B. J. Mater. Sci., **55** (2020) 12274-12286. https://doi.org/10.1007/s10853-020-04906-x.
71. Wang Z., Dong Y., Li H., Zhao Z., Bin Wu H., Hao C., Liu S., Qiu J., Lou X. W. - Enhancing lithium-sulphur battery performance by strongly binding the discharge products on amino-functionalized reduced graphene oxide. Nat. Commun., **5** (2014) 5002. https://doi.org/10.1038/ncomms6002.
72. Wei Z. Q., Dai X. C., Hou S., Li Y. B., Huang M. H., Li T., Xu S., Xiao F. X. - Branched polymer-incorporated multi-layered heterostructured photoanode: precisely tuning directional charge transfer toward solar water oxidation. J. Mater. Chem. A, **8** (2020) 177-189. https://doi.org/10.1039/C9TA11579J.
73. Xuyen N. T., Ting J. M. - Hybridized 1T/2H MoS_2 having controlled 1T concentrations and its use in supercapacitors. Chem. Eur. J., **23** (2017) 17348-17355. https://doi.org/10.1002/chem.201703690.
74. Chao Y., Jalili R., Ge Y., Wang C., Zheng T., Shu K., Wallace G. G. - Self-assembly of flexible free-standing 3D porous MoS_2-reduced graphene oxide structure for high-performance lithium-ion batteries. Adv. Funct. Mater., **27** (2017) 1700234. https://doi.org/10.1002/adfm.201700234.
75. Gao Z., Li M., Wang J., Zhu J., Zhao X., Huang H., Zhang J., Wu Y., Fu Y., Wang X. - Pt nanocrystals grown on three dimensional architectures made from graphene and MoS_2 nanosheets: highly efficient multifunctional electrocatalysts toward hydrogen evolution and methanol oxidation reactions. Carbon, **139** (2018) 369-377. https://doi.org/10.1016/j.carbon.2018.07.006.
76. Wang J. G., Liu H., Zhou R., Liu X., Wei B. - Onion-like nanospheres organized by carbon encapsulated few-layer MoS_2 nanosheets with enhanced lithium storage performance. J. Power Sources, **413** (2019) 327-333. https://doi.org/10.1016/j.jpowsour.2018.12.055.
77. Kandhasamy D. M., Mareeswaran P. M., Chellappan S., Namasivayam D., Aldahish A., Chidambaram K. - Synthesis and photoluminescence properties of MoS_2/graphene heterostructure by liquid-phase exfoliation. ACS Omega, **7** (2022) 629-637. https://doi.org/10.1021/acsomega.1c05250.
78. Zhang F., Tang Y., Liu H., Ji H., Jiang C., Zhang J., Zhang X., Lee C. S. - Uniform incorporation of flocculent molybdenum disulfide nanostructure into three dimensional porous graphene as an anode for high-performance lithium ion batteries and hybrid supercapacitors. ACS Appl. Mater. Interfaces, **8** (2016) 4691-4699. https://doi.org/10.1021/acsami.5b11705.
79. Ali G. A. M., Thalji M. R., Soh W. C., Algarni H., Chong K. F. - One-step electrochemical synthesis of MoS_2/graphene composite for supercapacitor application. J. Solid State Electrochem., **24** (2020) 25-34. https://doi.org/10.1007/s10008-019-04449-5.
80. Liu S., Zhang X., Shao H., Xu J., Chen F., Feng Y. - Preparation of MoS_2 nanofibers by electrospinning. Mater. Lett., **73** (2012) 223-225. https://doi.org/10.1016/j.matlet.2012.01.024.
81. Hamelin A., Vitanov T., Sevastyanov E., Popov A. - The electrochemical double layer on sp metal single crystals: the current status of data. J. Electroanal. Chem. Interfacial Electrochem., **145** (1983) 225-264. https://doi.org/10.1016/S0022-0728(83)80085-0.
82. Pech D., Brunet M., Durou H., Huang P., Mochalin V., Gogotsi Y., Taberna P. L., Simon P. - Ultrahigh-power micrometre-sized supercapacitors based on onion-like carbon. Nat. Nanotechnol., **5** (2010) 651-654. https://doi.org/10.1038/nnano.2010.162.